

REPORT DOCUMENTATION PAGE			Form Approved OMB No. 0704-0188	
Public reporting burden for this collection of information is estimated to average 1 hour per response, including the time for reviewing instructions, searching existing data sources, gathering and maintaining the data needed, and completing and reviewing this collection of information. Send comments regarding this burden estimate or any other aspect of this collection of information, including suggestions for reducing this burden to Department of Defense, Washington Headquarters Services, Directorate for Information Operations and Reports (0704-0188), 1215 Jefferson Davis Highway, Suite 1204, Arlington, VA 22202-4302. Respondents should be aware that notwithstanding any other provision of law, no person shall be subject to any penalty for failing to comply with a collection of information if it does not display a currently valid OMB control number. PLEASE DO NOT RETURN YOUR FORM TO THE ABOVE ADDRESS.				
1. REPORT DATE (DD-MM-YYYY) 30-06-2006		2. REPORT TYPE final report		3. DATES COVERED (From - To) 15-04-2005 - 31-03-2006
4. TITLE AND SUBTITLE A biomolecular motor-powered biosensor for remote detection scenarios		5a. CONTRACT NUMBER		
		5b. GRANT NUMBER FA9550-05-1-0274		
		5c. PROGRAM ELEMENT NUMBER		
6. AUTHOR(S) Henry Hess (Principal Investigator) hhess@u.washington.edu, hhess@mse.ufl.edu		5d. PROJECT NUMBER		
		5e. TASK NUMBER		
		5f. WORK UNIT NUMBER		
7. PERFORMING ORGANIZATION NAME(S) AND ADDRESS(ES) University of Washington Office of Sponsored Programs 1100 NE 45 th Street, Suite 300 Seattle WA 98105-0000 (206) 543-4043		8. PERFORMING ORGANIZATION REPORT NUMBER		
9. SPONSORING / MONITORING AGENCY NAME(S) AND ADDRESS(ES) USAF, AFRL N/Defense Advanced Research AF Office of Scientific Research Projects Agency (DARPA) 875 N. Randolph Str. RM 3112 Arlington, VA 22203 Valarie I. Hall 703-696-9736 Valarie.hall@afosr.af.mil		10. SPONSOR/MONITOR'S ACRONYM(S)		
		11. SPONSOR/MONITOR'S REPORT NUMBER		
12. DISTRIBUTION / AVAILABILITY STATEMENT Approve for Public Release: Distribution Unlimited.		AFRL-SR-AR-TR-06-0298		
13. SUPPLEMENTARY NOTES Program Manager: Dr. Hugh DeLong, AFOSR/NL, (703) 696-7722, hugh.delong@afosr.af.mil				
14. ABSTRACT The project is part of a collaborative effort between Sandia, the Naval Research Lab, the Albert Einstein Medical College, the ETH Zurich and the U. of Washington/U. of Florida to design a biomolecular motor-powered biosensor for remote detection of chem./bio agents under the auspices of the DARPA-DSO Biomolecular Motors program. The project is continued by the PI at the U. of Florida under grant FA9550-05-1-0366. Significant advances have been made in the capture of analytes by and controlled activation of molecular shuttles powered by biomolecular motors, as well as their longterm-storage and simulation of performance. A testbed mimicking remote detection by LIDAR has been developed and applied. The project resulted in 5 journal publications and 9 oral presentations at national conferences and departmental seminars (6 invited) and the training of several students and postdocs.				
15. SUBJECT TERMS				
16. SECURITY CLASSIFICATION OF:			17. LIMITATION OF ABSTRACT	18. NUMBER OF PAGES
a. REPORT	b. ABSTRACT	c. THIS PAGE		
				19a. NAME OF RESPONSIBLE PERSON
				19b. TELEPHONE NUMBER (include area code)

20060727343

Objectives: No changes.

Status of effort (see also comprehensive technical summary starting page 4):

By March 31, 2006 (the end date of the grant after a 3 month no-cost extension granted due to relocation of the laboratory), the status of the individual tasks is judged to be as follows:

Task 1.1- 100% completed: Demonstrate analyte capture by Ab-MTs transported by kinesin motors (*page 4*).

Task 1.2 – 100% completed: Measure the analyte capture efficiency at 5%, 50%, and 100% of the maximum velocity of the Ab-MTs (*page 5-14*).

Task 1.3 – 100% completed: Measure the ATP release as function of illumination intensity and duration (*page 15*).

Task 2.1 – 80% completed: Design an optical testbed with focused beam illumination and point detection for a target distance of 3-10 feet, which mimics a LIDAR setup (*page 16-19*).

The completion of the task has been deferred to the performance period of the continuation grant FA9550-5-1-0366 (Aug. 05 – July 07). The reason for the deferrance is that in this collaborative effort between NRL, Sandia, ETH Zurich, U. of Washington and Albert Einstein College of Medicine, we had to focus on show-stoppers and performed additional work outlined below. Since we were able to perform critical measurements with the testbed described under Task 2.2, the deferrance did not cause any delay of the overall effort.

Task 2.2 – 100% completed: Design an optical testbed with area illumination and imaging detection for a target distance of 3-10 feet, which permits the simultaneous readout of a large number of biosensor devices over an area of $\sim 1 \text{ m}^2$ (*page 20-21*).

Additional Tasks performed as a result of a focus on the DARPA team progress:

3.1 Significant contributions have been made to the effort by our DARPA collaborators from Albert Einstein College of Medicine to develop storage methods for biomolecular motor-powered nanodevices (*page 22*).

3.2 A method for the computer-assisted design and prediction of performance of guiding structures has been developed in collaboration with Dr. Takahiro Nitta, Gifu University Japan (*page 23*).

Accomplishments/Highlights:

- The results of Task 1.1. have been published on the **Cover** of the March edition of "Small": S. Ramachandran, K-H. Ernst, G. D. Bachand, V. Vogel, H. Hess*: „Selective loading of kinesin-powered molecular shuttles with protein cargo and its application to biosensing", Small 2(3), 330-334 (2006).
- The results of Task 1.3 have been published: D. Wu, R. Tucker, H. Hess*: „Caged ATP – Fuel for Bionanodevices“, IEEE Transactions in Advanced Packaging, 28(4), 594-599 (2005).
- The wider impact of this work has been reviewed in "NanoToday": H. Hess* and G.D. Bachand*: "Biomolecular Motors", Materials Today (NanoToday supplement) 8(12) suppl. 1, 22-29 (2005), invited feature article
- The results of Task 3.1 have been published: R. Seetharam, Y. Wada, S. Ramachandran, H. Hess, P. Satir*: "Long-term storage of bionanodevices by freezing and lyophilization", Lab on a Chip 2006, DOI:10.1039/B601635A

Final Report "A biomolecular motor-powered biosensor for remote detection scenarios"

The results of Task 3.2 have been published: T. Nitta*, A. Tanahashi, M. Hirano, H. Hess*: "Simulating molecular shuttle movements: Towards computer-aided design of nanoscale transport systems", Lab on a Chip, DOI: 10.1039/b601754a, webpublished 5/31/06

Personnel Supported:

Henry Hess, PhD (PI) – Research Assistant Professor/Assistant Professor

Gregory Lee, PhD – Senior Fellow

Sujatha Ramachandran – Research Scientist

Allan Scott Phillips – Research Scientist

Robert Tucker – Undergraduate Researcher/Graduate Student

Jeffrey Edwards – Undergraduate Researcher

Julien Gratier – Graduate Student

Isaac Luria – Graduate Student

Parag Katira – Graduate Student

Ashutosh Agarwal – Graduate Student

Isaac Finger – Graduate Student

Interactions:

Invited oral presentation - H. Hess: "Biomolecular Motors: Engines for Nanotechnology", Seminar of the BioSecurity & NanoSciences Laboratory and the Center For Micro and Nano Technology, Lawrence Livermore National Laboratory, CA (2005)

Oral presentation - S. Ramachandran, D. Wu, T. Nitta, R. Tucker, A. Phillips, and H. Hess: "Nanobiodevices Integrating Biomolecular Motors", NSTI Nanotech 2005, Anaheim, CA (2005)

Invited oral presentation - H. Hess: "Exploiting the Force-Generating Properties of Microtubule Motors in Nanoscience", Experts Workshop on the Physics of Biological Force Generation, Institute for Complex Adaptive Matter, Snowmass, CO (2005)

Oral presentation - S. Ramachandran, K.-H. Ernst, C. Brunner, V. Vogel, H. Hess: „Designing Nanoscale Cargo Carriers: Selective Loading of Functionalized Microtubules with Diverse Targets“, MRS Spring Meeting, San Francisco, CA (2005)

Oral presentation - R. Tucker, S. Ramachandran, D. Wu, T. Nitta, H. Hess: "Bionanodevices Integrating Molecular Motors", 52nd International Symposium of the AVS, Boston (MA) 2005

Invited oral presentation - H. Hess: "Biomolecular Motors: Engines for Nanotechnology", Seminar of the Department of Pharmacology, University of California, Los Angeles, CA (2005)

Final Report "A biomolecular motor-powered biosensor for remote detection scenarios"

Invited oral presentation - H. Hess: "Biomolecular Motors: Engines for Nanotechnology", Seminar of the Materials Science and Engineering Department, University of Michigan, MI (2005)

Invited oral presentation - H. Hess: "Biomolecular Motors: Engines for Nanotechnology", Geometry, Graphics, Vision, Visualization/Visual Simulation (G2V2) Seminar, Department of Computer and Information Science and Engineering, University of Florida, FL (2006)

Invited oral presentation - H. Hess: "Filming the actions of bionanomotors with epi-fluorescence microscopy", 2006 Annual Joint Symposium, Florida Chapter of the AVS and Florida Society for Microscopy, Orlando, FL, (2006)

Discoveries, inventions, patent disclosures: None

Honors/Awards: 2005 Philip-Morris Research Prize (Henry Hess and Viola Vogel)

This award is a major german research prize (100 kEuro total) given annually to four teams. Viola Vogel and Henry Hess have been recognized for their contributions to Bionanotechnology.

Comprehensive technical summary of significant work accomplished:

Task 1.1: *Demonstrate analyte capture by Ab-MTs transported by kinesin motors.*

The methods and results are publicly accessible through: S. Ramachandran, K-H. Ernst, G. D. Bachand, V. Vogel, H. Hess: „Selective loading of kinesin-powered molecular shuttles with protein cargo and its application to biosensing”, *Small* 2(3), 330-334 (2006)

Abstract: Molecular shuttles, nanoscale biomolecular motor-driven transport systems, are a bio-inspired alternative to pressure-driven fluid flow or electroosmotic flow in micro- and nanofluidic systems. Significant progress has been made in directing the movement of such shuttles, in controlling the activation, and in loading some types of cargo. However, a generalized approach to selectively bind nanoscale cargo, such as proteins, viruses or inorganic nanoparticles, to a molecular shuttle is a pressing concern for researchers interested in the technological applications of active transport, since it enables the design of a variety of analytical devices. Here, we demonstrate that selective binding and subsequent transport of target proteins can be achieved by assembling a multi-layer structure consisting of streptavidin and biotinylated antibodies on a biotinylated microtubule, which can be transported by surface-immobilized kinesin motor proteins.

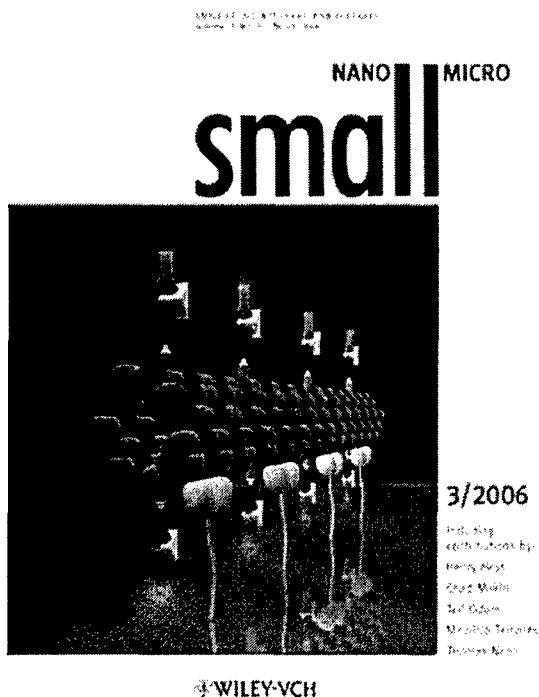


Figure 1: The cover picture illustrates a functionalized microtubule transported by surfaceadhered kinesin motor proteins. Through a streptavidin bridge, biotinylated antibodies are attached to the microtubule (outer diameter of 24 nm) and are able to capture antigens, such as the heart attack marker myoglobin. Successful capture is reported via the binding of fluorescently-labeled antibodies, which complete the double-antibody sandwich assay on the microtubule. The motor-driven, active transport of this nanoscale bioassay will enable further separation and concentration, as well as sensitive detection.

Task 1.2: Measure the analyte capture efficiency at 5%, 50%, and 100% of the maximum velocity of the Ab-MTs.

First, theoretical discussion on the velocity-dependence of the pick-up of analytes by microtubules in a flow-cell is given below. The effect of factors such as analyte size, analyte-surface interaction properties and the speed of microtubule movement can be understood by simple models. The analyte pick-up can be either by diffusion of analytes onto the microtubules, or the pick-up of surface bound analytes by moving microtubules. Both these mechanisms have been discussed below.

Nomenclature

l = length of MT ($10\mu\text{m}$)

D = Diffusion constant of analyte

C_{Sol} = Concentration of analytes in solution in particles/ μm^3

R = Radius of cylindrical boundary for diffusion (assumed to be the height of the compartment)

r_{MT} = radius of MT

t = time for analyte capture

N_{Sol} = Number of analytes captured from solution

δ_c = Thickness of diffusion boundary layer

δ = Thickness of velocity boundary layer

δ_c^* = Thickness of diffusion boundary layer at half length of MT

ν = Kinematic viscosity of solution

x = Distance from leading edge of MT

U = Velocity of MT gliding

C = constant (value=1.78)

h = Height of MT above the surface

$R_{analyte}$ = Radius of analyte

$L_r = 2 \times \text{reach of MT on either side}$

σ = Surface density of analytes in particles/ μm^2

N_{surf} = Number of analytes picked up from the surface

Analyte capture by diffusion:

The capture of analytes from solution by a microtubule can be described as diffusion to a semi-cylinder. For simplicity, we consider a semi-cylindrical compartment boundary encompassing the microtubule. (This should not change the diffusion flux as compartment boundaries are extremely far away from the microtubule and assuming a cylindrical enclosure would not affect the actual numbers greatly.) Thus, based on this the number of analytes captured by the microtubule from solution can be given by

$$N_{Sol} = \frac{\pi l D C_{Sol} * t}{\ln\left(\frac{R}{r_{MT}}\right)} \quad \dots \quad (1) \quad \dots$$

Standard diffusion equation to a hemi-Cylinder based on theory by Berg HC, Random walks in Biology.

Here we have made the two following important assumptions

1. That any analyte that reaches the microtubule is captured by it without any chance of unbinding.
2. The number of analytes captured in expected times of observation is much less than that required for saturation of all analyte binding sites on the microtubule.

Now, instead of the microtubule being stationary on the surface, assume that it is moving over it. Thus, what should be the effect of this motion on the analyte pick-up by microtubules as a function of their gliding velocity?

The effect of motion would be such that there is a constant replenishment of analytes in the solution above the microtubule. Now, the concentration of analytes shall be equal to that of the remaining solution at a distance smaller than the compartment boundaries (R). This distance can be given by the diffusion boundary layer. The thickness of this layer increases from the leading edge of the microtubule up to the trailing edge, but for sake of simplicity, we assume diffusion from a hemi-cylindrical layer of analytes at a distance equal to the boundary layer thickness at half length of the microtubule. This cylindrical layer would be at the same concentration as bulk solution and thus now the number of analytes captured can be given as (... I don't know how good this assumption is)

$$N_{Sol} = \frac{\pi l D C_{Sol} * t}{\ln\left(\frac{\delta_c^*}{r_{MT}}\right)} \quad \dots \quad (2) \quad \dots$$

Standard diffusion equation to a hemi-Cylinder based on theory by Berg HC, Random walks in Biology.

The diffusion boundary layer is related to the velocity boundary layer by the Schmidt number which if same as in case of a flat plate can be written as

$$\delta_c = \delta * \sqrt[3]{\frac{D}{\nu}} \quad \dots \quad (3) \quad \dots$$

Expr. 3.3-132 to 134, Transport Phen & Matl. Processing, Sindo Kou, 1996 J Wiley & Sons.

Where, the velocity boundary layer for flow along a long thin cylinder is given to be of the order of

$$\delta \propto x \left[\frac{v}{Ux \ln \left(\frac{4xv}{Cr_{MT}^2 U} \right)} \right]^{\frac{1}{2}} \quad \dots \quad (4) \quad \dots \quad \text{K. Stewartson, Q. Appl. Math. 13, 113 (1955)}$$

Thus the increase in the analyte capture by a moving microtubule compared to a stationary microtubule is given by

$$\frac{N_{Sol} \text{ for moving MT}}{N_{Sol} \text{ for stationary MT}} = \frac{\ln \left(\frac{R}{r_{MT}} \right)}{\ln \left(\frac{\delta_C^*}{r_{MT}} \right)} \quad \text{where } \delta_C^* \text{ is } \delta_C \text{ at } x = 5\mu\text{m} \text{ assuming avg. length}$$

of MT to be $l = 10\mu\text{m}$. $\dots \quad (5)$

Thus from (3), (4) and (5) we can get an approximate velocity dependence of analyte capture by a moving microtubule.

Figure 2 below shows this percentage increase of analyte pick-up as a function of microtubule velocity for three sizes of analytes: 1000nm, 40nm, 5nm.

Thus it can be clearly seen that the effect of speed on MT loading is higher for particles with larger sizes or smaller diffusion coefficients. Yet, for particles with extremely small diffusion coefficients, the loading of stationary MTs is itself very less, that a possible 50% increase also may not cause a great difference to the number of analytes captured on a microtubule.

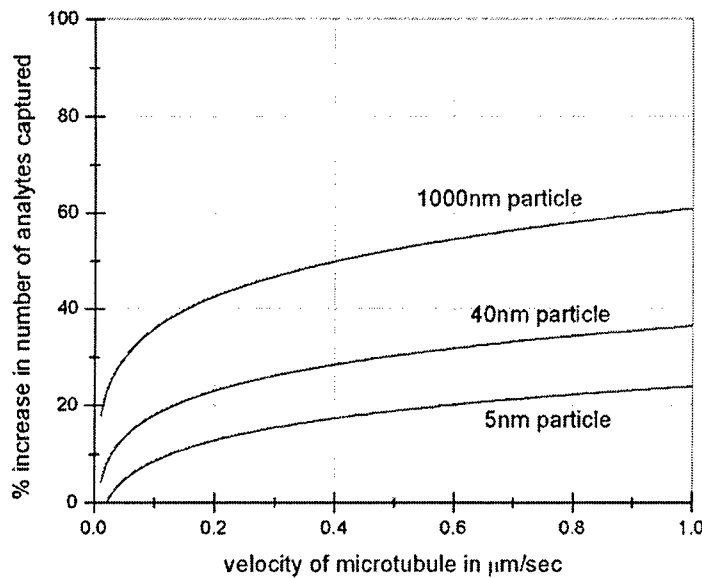


Figure 2. The figure shows the effect of MT speed on loading obtained by combining expressions (3), (4), (5)

In figure 3, the number of analytes that would be picked up from the solution as a function of MT velocity is shown for three different sizes of analytes. From the plots it can be seen that the effect of velocity is not extremely prominent. For example, even though at very high MT speed, for a 1000nm particle, the expected increase in the pick-up is about 50%. But when actual numbers are considered the number of analytes picked up in a 1000sec increases from 0.1 to 0.15 from stationary to high speeds.

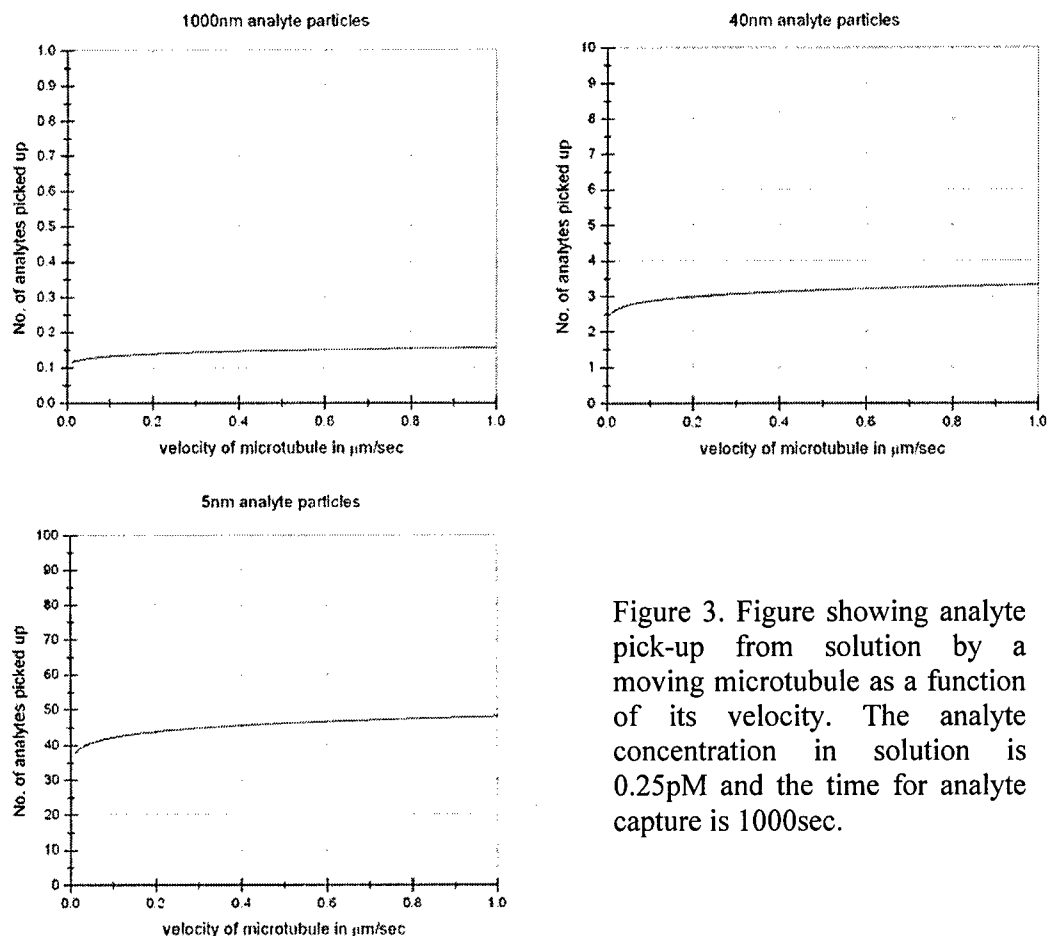


Figure 3. Figure showing analyte pick-up from solution by a moving microtubule as a function of its velocity. The analyte concentration in solution is 0.25pM and the time for analyte capture is 1000sec.

The main effect of moving microtubule and microtubule speed can be seen in the pick up of analytes from the surface of the cell. This pick-up method is explained in the next section.

Analyte capture by pick-up from surface:

This kind of pick-up is possible only by MTs gliding on the surface of the flow cell. When gliding MTs encounter loosely adsorbed analyte particles on the surface, the binding between functionalized groups on MTs and analytes being much more specific and strong, the MTs pick them off the surface. The reach of the microtubules on both sides is a function of the analyte size. This can be seen from the following figure 4.

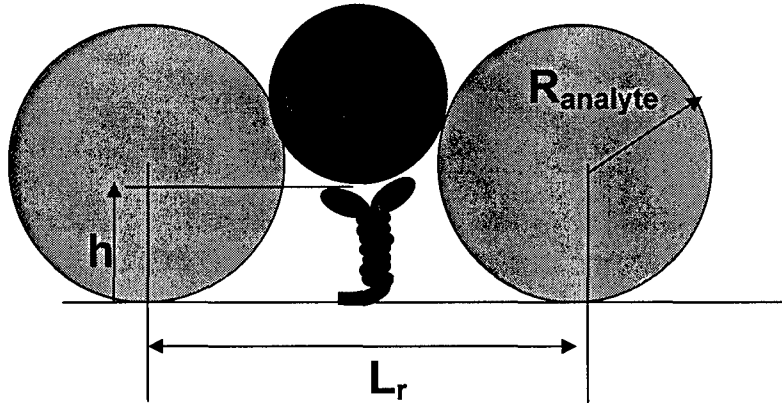


Figure 4: Geometry of surface pick-up

The reach of the MT on the sides is given by

$$L_r = 2\sqrt{(R_{analyte} + r_{MT})^2 - [R_{analyte} - (r_{MT} + h)]^2} \quad \dots \quad (6)$$

Thus, if a MT is gliding on a surface, it will pick up any analyte particles stuck on the surface which are at a distance of $L_r/2$ on either side of it. Now if the surface density of the analytes is a constant, then on an average the number of analytes encountered by the MT in a given time t will be given by

$$N_{Surf} = \sigma \cdot A \quad \dots \quad (7)$$

And the area for pick-up for the traversing MT is given by

$$A = L_r \cdot (Ut)$$

Thus $N = \sigma \cdot L_r \cdot (Ut)$ or

$$N = \sigma \cdot 2\sqrt{(R_{analyte} + r_{MT})^2 - [R_{analyte} - (r_{MT} + h)]^2} \cdot U \cdot t \quad \dots \quad (8)$$

Here we assume that the time for binding between analyte and MT is extremely small and thus the binding is almost instantaneous, i.e. the MT speed does not affect the efficiency of pick up and the MT picks up all analytes in its way.

Thus, from equation (8) we can plot the dependence of analyte pick-up from surface to the MT speed (Figure 5). The figure shows pick-up for three sizes 1000nm, 40nm and 5nm of analytes. (For the 5nm analyte particles we assume them to move just next to the surface i.e. $h=0$ nm. For the other two case we assume avg. height of MT above surface to be 20nm.) For this figure, we assume a .25pM concentration of analytes settled completely on the surface and a total time before observation of 1000 seconds. The overlapping of Mt on its own path or other MTs on this one's path can be neglected as the area overlapped would still be extremely small.

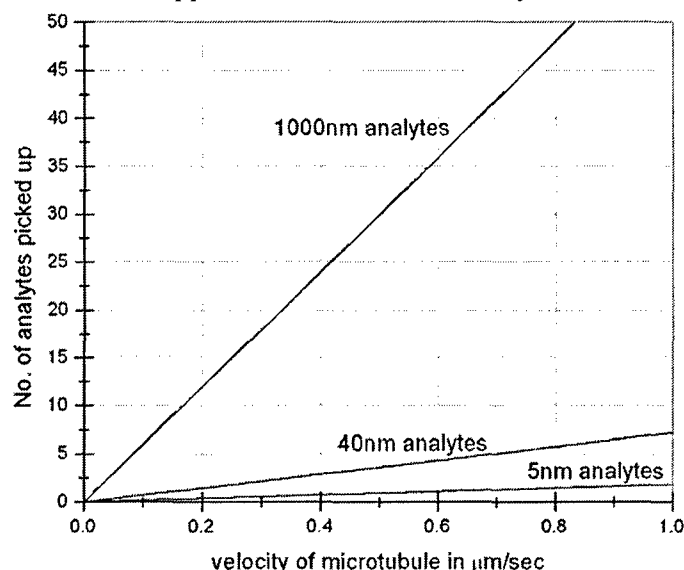


Figure 5: Number of analytes picked up by moving microtubules in a time of 1000sec and at a analyte surface density of 0.03 analyte particles per μm^2 .

Therefore even in this situation the gliding of the MT on the surface favors the pick-up of larger size analytes than smaller ones. Also, since the pick up of large analytes is very low by diffusion, the pick-up of adsorbed analytes from surface is a much more dominating mechanism for analyte transport of large size analytes. (Depending on their concentration in the solution and surface adsorption coefficient)

Summary of predicted results:

Based on the above discussions, we can compare the effect of velocity, the size of analytes, and the method of analyte pick-up on the number of analytes picked up by a microtubule. In figure 6, we give a plot of analytes picked up by microtubules as a function of velocity for 3 different sizes. Here we compare the number picked up by either method, i.e. from surface or from solution by the microtubule. For this purpose we consider a solution with analyte concentration of 0.25pM and two cases: 1. when all particles are in the solution and none is adsorbed onto the surface, 2. when all particles

from the solution are adsorbed onto the surface and then MTs glide over the surface and pick them up. The comparison between these 2 cases is shown for sizes 1000nm, 40nm and 5nm.

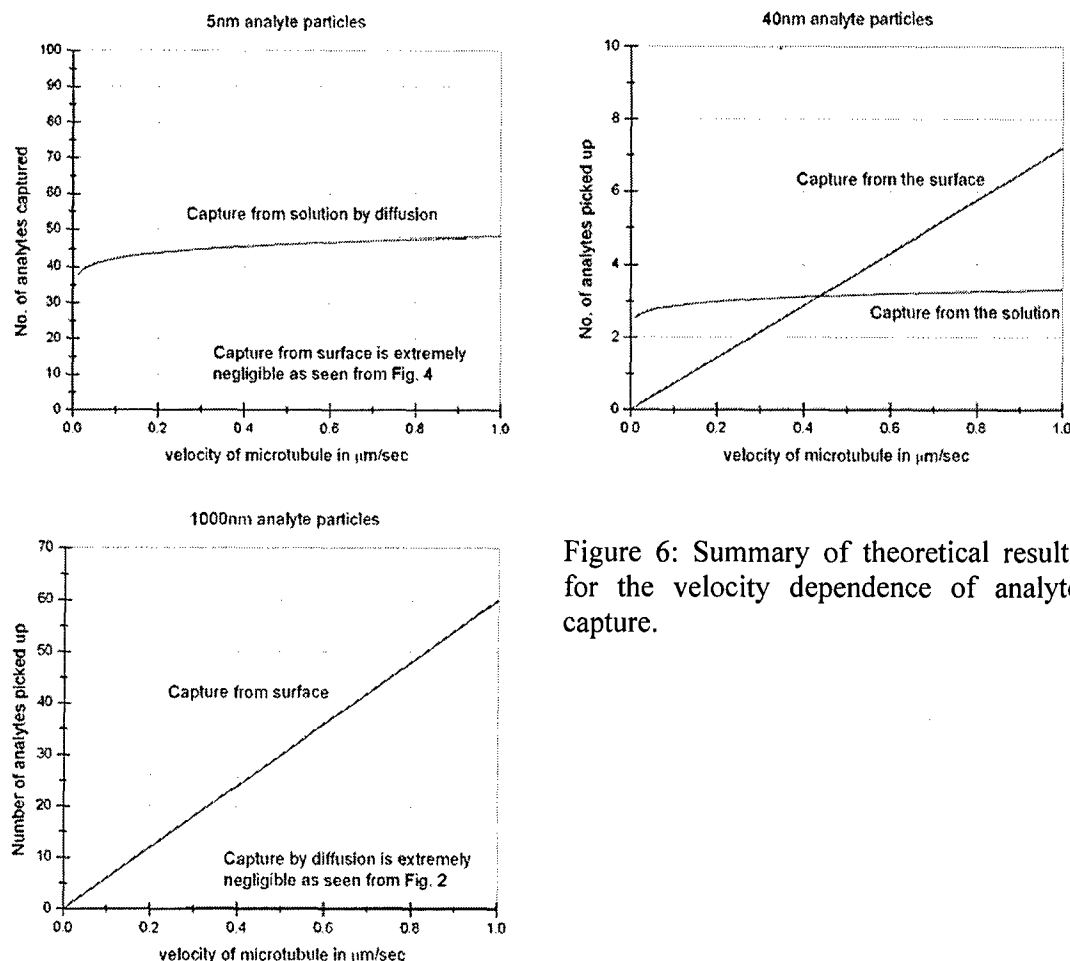


Figure 6: Summary of theoretical results for the velocity dependence of analyte capture.

In summary, analyte capture depends in a nontrivial way on the velocity of the microtubule, since two mechanisms (capture from surface, capture from solution) contribute to capture. While capture from surface has a linear velocity dependence in all case, capture from solution becomes only marginally more efficient for microtubules moving at top speed vs. stationary microtubules. The relative importance of the mechanism varies for 5 nm particles (proxy for proteins – diffusion capture predominant), 40 nm particles (proxy for viruses – both mechanisms can contribute substantially), and 1000 nm particles (proxy for bacteria – capture from surface predominant). However, the specific propensity of an analyte to adhere to the surface can modify this balance. As a rule, a high microtubule velocity is desirable, since it increases analyte capture in all cases.

Experimental results:

Attachment of 40nm beads to microtubules as a function of microtubule speed.

As a part of the long term goal of studying the variation of attachment and transport of cargo of varying sizes by kinesin-microtubule system as a function of microtubule speed, experiments were carried out with 40 nm microspheres as cargo. Before the variation of attachment and transport with speed could be studied, the right concentrations of these beads in a flow cell had to be chosen for an unimpeded transport as well as a good attachment rate.

Experimental details: Biotinylated microtubules were prepared by polymerizing biotin labeled tubulin (Cytoskeleton Inc.). Polymerization was performed in BRB80 (80 mM PIPES, 1 mM MgCl₂, 1 mM EGTA, pH 6.8 with KOH), 1mM GTP, 4mM MgCl₂ and 5% DMSO at 37°C for 30 min. Biotinylated microtubules were then stabilized with BRB80 and 10uM taxol to be stored at room temperature. No experiments were done with microtubules more than 24 hours old. For imaging purposes and attachment of biotinylated cargo, these were first coated with excess fluorescent streptavidin (STV-AF-568, Invitrogen Inc.) and then washed with motility solution without microtubules to get rid of unattached streptavidin.

In the standard inverted gliding motility assay, the following was the order of infusion of solutions into the flow-cell.

1. Casein solution (0.5 mg/ml in BRB80)
2. Kinesin solution (20 fold dilution into casein solution containing varying percentages of ATP)
3. Motility solution (5 times dilution of stabilized microtubules containing 10uM taxol, 20mM d-glucose, .02 mg/ml glucose-oxidase, .008 mg/ml catalase, 0.5% DTT and varying amounts of ATP.)
4. Streptavidin (5nM diluted into motility solution without microtubules)
5. 3 washes of motility solution without microtubules.

The flow cell was then mounted on the Nikon-eclipse fluorescence microscope for checking for motility of microtubules using 100X oil objective. Images were collected using an Andor EMCCD camera and Lambda SC smart shutter which were controlled by an in-house developed LABVIEW program. The flow cell was exposed to Hg arc lamp illumination only for the period when camera was acquiring the images to avoid excess photo-exposure.

6. Keeping the microtubules in focus 40nm bead solution was infused after normal motility was attained. For all experiments, the beads were first diluted into a Block-Aid solution (Invitrogen Inc.) with anti-fade agents and then into the motility solution without microtubules. They were sonicated for five minutes to break bead agglomerations.

The beads attached to moving microtubules clearly stand out from the rest of the beads which are either adsorbed to the surface and not moving, or are bouncing on and off the

surface. The beads attached to microtubules always stay in focus and show smooth motion on the surface. These are also verified by switching between filters and seeing if a moving microtubule is present at the point where the bead in question is.

The attached and moving beads in an 80 μ m by 80 μ m field of view are counted and are divided the total moving microtubules present in the same field of view to get the attachment rate.

Results and Discussion

Effective transport of 40nm fluorescent beads significantly depends on the density of beads. It was found out that at concentrations more than 500pM (1/1000 dilution), microtubules were coated with particles but the transport of these loaded microtubules was significantly hindered. At 50pM concentration (1/10000 dilution) though there was normal motility of loaded microtubules, their breakage rate was high (due to the presence of a large amount of fluorescent groups). Also at concentrations less than 10pM (1/50000 dilution), there was a poor attachment rate of beads to microtubules.

All experiments were carried out at 25pM concentration (1/20000 dilution) of beads. The speed of microtubules was varied by controlling the ATP concentration. Data were collected for 4 MT speeds: 520nm/s (Fig. 7), 352nm/s (Fig. 8), 146nm/s (Fig. 9) and 56nm/s (Fig. 10). The scale bar is 10 μ m.



Fig7: MT speed = 520 nm/s; time interval between images = 4s

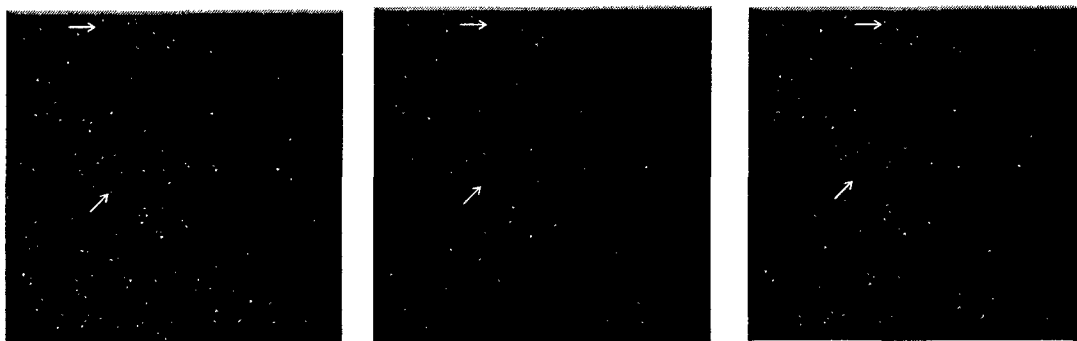


Fig 8: MT speed = 352 nm/s; time interval between images = 15 s

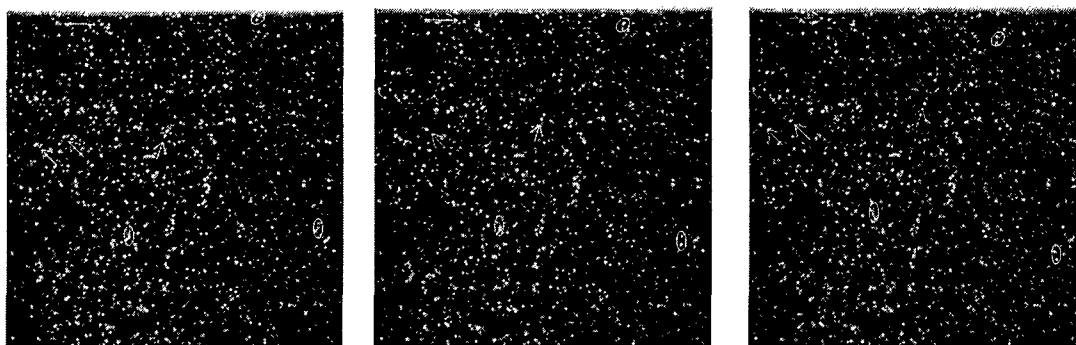


Fig 9: MT speed = 146 nm/s; time interval between images = 24s

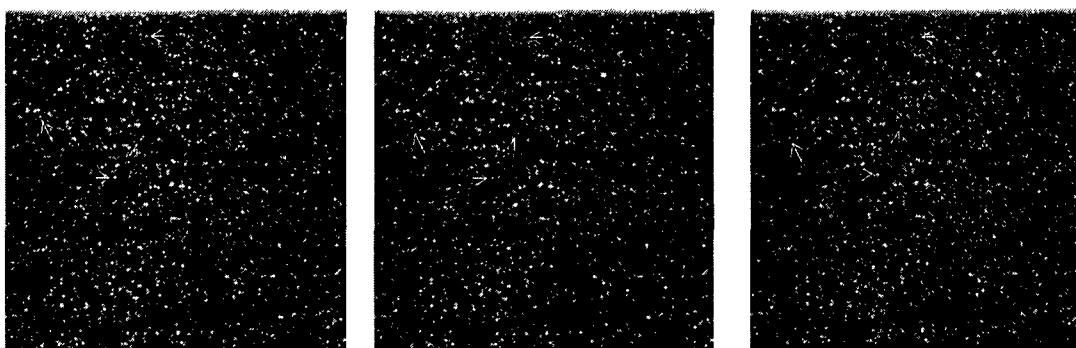


Fig 10: MT speed = 56 nm/s; time interval between images = 40s

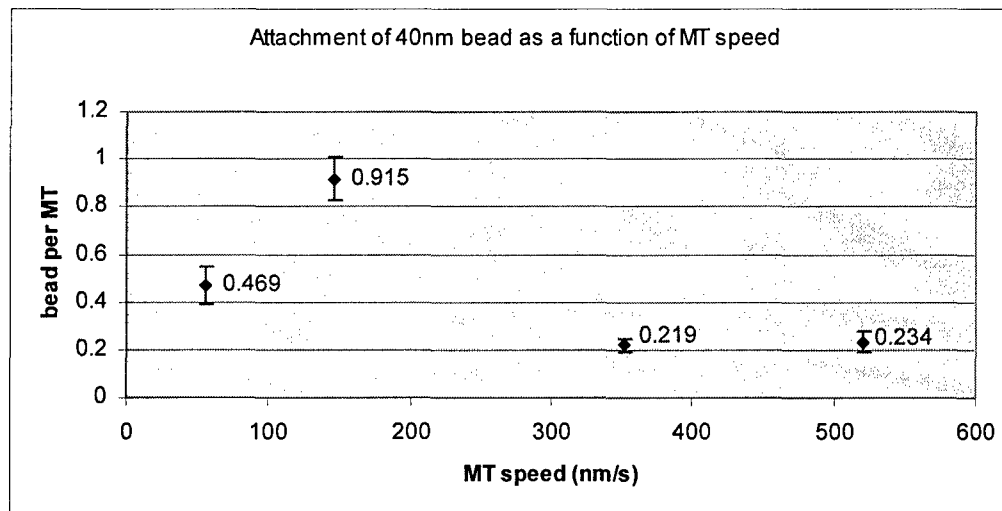


Fig. 11: Capture of 40 nm beads as function of MT velocity.

In summary, the experimental data showed that capture efficiency depended only weakly on speed, even though the data did not reproduce the theoretically predicted monotonous increase. Additional experiments (data not shown) for protein capture, also showed no acceleration of capture within the experimental error (+30%). Consequently, the design of the device and the choice of the microtubule velocity are not critically affected by considerations of velocity-dependent analyte capture.

Task 1.3: Measure the ATP release as function of illumination intensity and duration.

The methods and results are publicly accessible through: D. Wu, R. Tucker, H. Hess: „Caged ATP – Fuel for Bionanodevices“, IEEE Transactions in Advanced Packaging, 28(4), 594-599 (2005).

Abstract: Micro- and nanodevices require the controlled delivery of energy to power a variety of processes. The current paradigm of connecting a miniaturized device to a set of macroscopic auxiliary devices, such as power supplies or pumps, for the delivery of electrical and mechanical energy needs to be replaced to enable the design of stand-alone, integrated bionanodevices with applications in remote biosensing or nanomedicine. Biological nanomachines, such as the motor protein kinesin, can efficiently convert energy stored in chemical compounds, in particular ATP, into mechanical work. This ability is an attractive feature of hybrid devices powered by biomolecular motors, since it removes the need for the storage and conversion of electrical energy. The consequences are a simplified fabrication process and packaging, leading to higher yields and lower costs, and the broadening of the applications, which can now include field-deployable nanodevices. Here, the potential of caged ATP as fuel for such engineering applications is discussed. Caged ATP can be stored in the buffer solution of a bionanodevice, “uncaged” by UV light, and utilized as fuel by many enzymes to catalyze chemical changes or power active transport. We demonstrate that DMNPE-caged ATP can be stored in sufficient amounts in a typical device, and that the activation can be triggered with a UV-lamp or even sunlight.

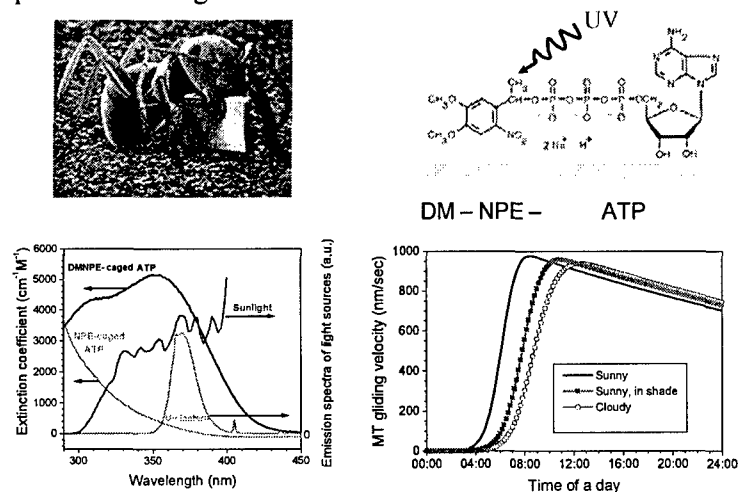


Figure 12: Top left – “Smart Dust” devices, in contrast to microfluidic devices with macroscopic interfaces, do not provide buttons and dials for external control. Top right – Caged ATP, which can be activated by photolysis with UV photons, has proven to be an excellent choice for controlling kinesin motor-powered microdevices. Bottom left – DMNPE-caged ATP is the optimal choice among caged ATP variants, due to its large spectral overlap with sunlight and standard UV light sources. Bottom right – Based on the measured absorption cross sections and quantum efficiencies, we predict that even on a cloudy day in Seattle sunlight is sufficient to fully activate our “smart dust” devices by noon.

Task 2.1: Design an optical testbed with focused beam illumination and point detection for a target distance of 3-10 feet, which mimics a LIDAR setup.

Typical UV-LIDAR systems are based on a frequency-tripled Nd:YAG laser system with a repetition rate of 20-30 Hz and a pulse energy of 20-100 mJ at 355 nm. The laser beam is widened by a beam expander and directed onto the target where the beam diameter has increased to 200 mm at a standoff distance of 500 m. A telescope with an aperture diameter of 20-80 cm collects the fluorescence light and directs it onto photomultipliers or intensified CCD, which are gated with a time resolution of 10 ns (1.5 m spatial resolution). Cutting edge UV laser diodes enable novel designs with a significant reduction in size and power requirements. Time-resolved gating minimizes the impact of sunlight on the SNR. See Hargis, P., A. Lang, R. Schmitt, T. Henson, J. Daniels, D. Jordan, K. Schrodner, and I. Shokair. 1998. Sandia Multispectral Airborne LIDAR for UAV Deployment. SAN098-2386C.

Due to time-resolved gating ability, the performance of traditional LIDAR does not significantly vary between daytime and nighttime. Essentially, the energy delivered by the sun (a low brightness cw source) is reduced by a factor of 10^8 through the 10 ns open time of the detector.

Based on the specifications of contemporary LIDAR systems listed above, we define the canonical “reference LIDAR” with the following specifications: Nd:YAG laser with 30 Hz repetition rate, and pulse energies of 200 mJ at 1064 nm (fundamental), 100 mJ at 532 nm (second harmonic), 30 mJ at 355 nm (third harmonic). The laser beam divergence is assumed to be 0.4 mrad (8” spot size at 500 m standoff). The detection system has a 30 cm diameter collection mirror (previously we assumed an 80 cm mirror), utilizes gating electronics with 2 ns minimum resolution, and a state-of-the-art gated CCD detector with 50% quantum efficiency (e.g. Andor DH K712 Gen III Filmless).

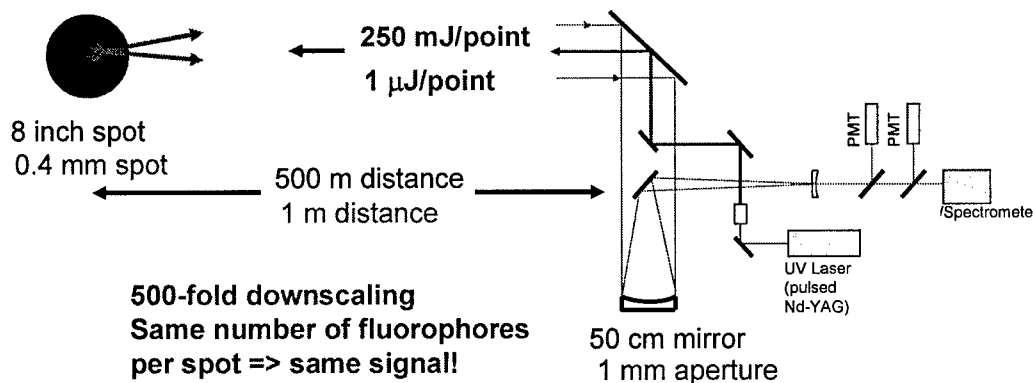


Figure 13: Downscaling of a LIDAR system to a testbed enables the direct comparison of detection sensitivity.

We further define the Fluorescence sensing equation, which specifies the scaling of the the signal to noise ratio (SNR) as function of distance, target, and system properties. While certain aspects of the complex situation in the field (e.g. absorption/scattering in the air) are neglected, the equation is meant to enable the

prediction of the approximate performance of a fluorescent target in a LIDAR detection situation based on its performance in a downscaled testbed.

The SNR is determined by the photon flux P reaching the detector, and the ability of the detector to convert this flux into a signal above the detector noise for a given exposure time. The photon flux entering the detector scales as:

$$P = I_{\text{exc-target}} \times F_{\text{QD-VNP}} \times N_{\text{QD-VNP/device}} \times N_{\text{device/spot}} \times \text{CE} \quad (1)$$

With: $I_{\text{exc-target}}$ - Intensity of excitation light at target location
 $F_{\text{QD-VNP}}$ - Fluorescent brightness emitted for each tag
 $N_{\text{QD-VNP/device}}$ - Number of tags per device
 $N_{\text{device/spot}}$ - Number of devices per spot
CE – collection efficiency for emitted light

In a LIDAR system, the average excitation intensity is given by:

$$I_{\text{exc-target}} = E \times f_{\text{repetition}} / d^2 \theta^2 = E \times f_{\text{repetition}} / A \quad (2)$$

Where: E – pulse energy, $f_{\text{repetition}}$ - repetition rate, d – standoff distance,
 θ – beam divergence, A – spot size

For the reference LIDAR system defined above, we obtain

$$I_{\text{exc-target}} = 0.03 \text{ J} \times 30 \text{ Hz} / 0.16 \text{ (mrad)}^2 / d^2 = 5.6 \text{ MW} / d^2 \quad (3)$$

The collection efficiency CE is given by:

$$\text{CE} = \pi/4 \times D^2 / 4\pi d^2 = D^2 / 16d^2 \quad (4)$$

Where : D – diameter of collection optics, d – standoff distance

Putting (2) and (4) into (1) yields

$$P = E \times f_{\text{repetition}} / d^2 \theta^2 \times F_{\text{QD-VNP}} \times N_{\text{QD-VNP/device}} \times N_{\text{device/spot}} \times D^2 / 16d^2$$

Using the specifications for the LIDAR system above:

$$P = 5.6 \text{ MW} / d^4 \times D^2 / 16 \times F_{\text{QD-VNP}} \times N_{\text{QD-VNP/device}} \times N_{\text{device/spot}}$$

$$P_{\text{LIDAR}} = 5.6 \text{ MW} \times 0.09 \text{ m}^2 / d_{\text{LIDAR}}^4 / 16 \times F_{\text{QD-VNP}} \times N_{\text{QD-VNP/device}} \times N_{\text{device/spot}}$$

In comparison, the testbed utilizes a cw-source delivering $P_{\text{exc}} \sim 60 \text{ mW}$ with a beam divergence of $\theta = 0.043 \text{ rad}$ at the target, collection optics with 2.5 cm diameter:

$$P = P_{\text{exc}} / d^2 \theta^2 \times F_{\text{QD-VNP}} \times N_{\text{QD-VNP/device}} \times N_{\text{device/spot}} \times D^2 / 16d^2$$

Final Report “A biomolecular motor-powered biosensor for remote detection scenarios”

$$P_{\text{testbed}} = 32 \text{ W} \times 6.25 \times 10^{-4} \text{ m}^2 / d_{\text{testbed}}^4 / 16 \times F_{\text{QD-VNP}} \times N_{\text{QD-VNP/device}} \times N_{\text{device/spot}}$$

Since the photon flux to the detectors in testbed and LIDAR system depends in the same way on target properties and stand-off distance, we can define an equivalent testbed distance for a given LIDAR standoff distance by equating P_{LIDAR} with P_{testbed} and solving for $d_{\text{LIDAR}} / d_{\text{testbed}}$:

$$E \times f_{\text{repetition}} / d_{\text{LIDAR}}^2 \theta_{\text{LIDAR}}^2 \times F_{\text{QD-VNP}} \times N_{\text{QD-VNP/device}} \times N_{\text{device/spot}} \times D_{\text{LIDAR}}^2 / 16 d_{\text{LIDAR}}^2 \\ = P_{\text{exc}} / d_{\text{TB}}^2 \theta_{\text{TB}}^2 \times F_{\text{QD-VNP}} \times N_{\text{QD-VNP/device}} \times N_{\text{device/spot}} \times D_{\text{TB}}^2 / 16 d_{\text{TB}}^2$$

$$E \times f_{\text{repetition}} / d_{\text{LIDAR}}^4 \theta_{\text{LIDAR}}^2 \times D_{\text{LIDAR}}^2 = P_{\text{exc}} / d_{\text{TB}}^4 \theta_{\text{TB}}^2 \times D_{\text{TB}}^2$$

$$d_{\text{LIDAR}}^4 / d_{\text{TB}}^4 = E \times f_{\text{repetition}} / P_{\text{exc}} \times \theta_{\text{TB}}^2 / \theta_{\text{LIDAR}}^2 \times D_{\text{LIDAR}}^2 / D_{\text{TB}}^2$$

$$d_{\text{LIDAR}} / d_{\text{testbed}} = (5.6 \text{ MW} \times 0.09 \text{ m}^2 / 32 \text{ W} / 6.25 \times 10^{-4} \text{ m}^2)^{0.25}$$

$$d_{\text{LIDAR}} / d_{\text{testbed}} = (5.6 \times 0.09 / 32 / 6.25 \times 10^{-4})^{0.25} = (0.25 \times 10^{-8})^{0.25}$$

$$d_{\text{LIDAR}} / d_{\text{testbed}} = 70$$

The ideal scaling testbed ratio would be 500, so that a 500 m LIDAR stand-off distance corresponds to a 1 m testbed stand-off distance. This increase of a factor 7 can be achieved by simultaneous reduction of the testbed aperture and the cw-source power. However, it is critical to remember that the number of devices per spot $N_{\text{device/spot}}$ is limited to one in the testbed (since the size of one spot equals the size of the device), while $N_{\text{device/spot}}$ is expected to be 10-100 in the LIDAR system. Since the LIDAR excitation is pulsed with a frequency of 30 Hz, the exposure time in the testbed (using cw illumination) has to be adjusted in full increments of 33 ms, in order to permit a meaningful comparison of average excitation energies delivered. Prior published experiments related to remote fluorescence detection (Simonson, Simard) typically average the signal over 200-300 laser shots (= 10 s collection time). However, single shot detection is eminently desirable for rapid evaluation of a large area covered by smart dust biosensors and is pursued here. It should also be remembered, that as the LIDAR stand-off distance increases, the reduced excitation intensity (due to expansion of the beam) is compensated by a proportionally increased number of devices interrogated. The collected LIDAR signal thus depends only on the square of the standoff distance.

These calculations set the stage for comparing the performance of the testbed to typical LIDAR systems. A publication describing the calculations and quantitative comparison in detail is in preparation and will be referenced in the final report of the continuation grant FA9550-05-1-0366.

However, in addition to the downscaled replication of a LIDAR setup, the design an optical testbed with focused beam illumination and point detection for a target distance of

Final Report “A biomolecular motor-powered biosensor for remote detection scenarios”

3-10 feet also was pursued to provide a sensitive, handheld device for stand-off detection of fluorescence. The basic design of the initial setup is displayed in figure 14.

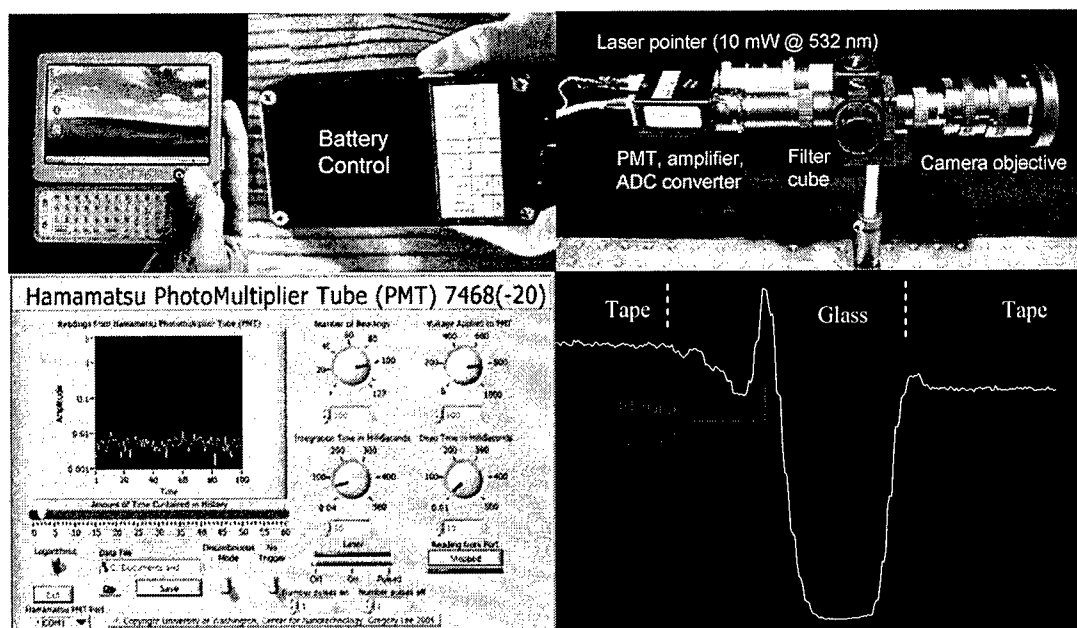


Figure 14: Top left – A handheld, Windows-compatible pocket PC can run the labview based data acquisition software. Batteries and control electronics for laser and detector fit into a palm-size housing. Top right – The optical device consists of a photomultiplier tube with integrated amplifier and ADC converter (RS232 bus, Hamamatsu PMT 7468-20), a 532 nm laser (Wickedlasers Inc.) and the optics with an overall length of 10 inches and a weight of 1 pound. Bottom left – A labview-based graphical user interface has been designed to control the device modules and read out the data. Bottom right – The presence of individual optical tags (Nile-red FluoSphere, Molecular Probes Inc., Product nr. F-8819) can be detected.

A significant amount of work had to be performed to design the control software. After initial tests, we succeeded in imaging individual optical tags. However, the signal to noise ratio did not conform to our expectations, and we found significant autofluorescence from the camera objective, which interfered with our measurements.

We are currently redesigning the optical setup to achieve the initially proposed specifications. Once these problems have been overcome, we will summarize the results and the design in a publication.

As mentioned above, the completion of the task has been deferred to the performance period of the continuation grant FA9550-5-1-0366 (Aug. 05 – July 07). The reason for the deferrance is that in this collaborative effort between NRL, Sandia, ETH Zurich, U. of Washington and Albert Einstein College of Medicine, we had to focus on show-stoppers and performed additional work outlined below. Since we were able to perform critical measurements with the testbed described under Task 2.2, the deferrance did not cause any delay of the overall effort.

Task 2.2: Design an optical testbed with area illumination and imaging detection for a target distance of 3-10 feet, which permits the simultaneous readout of a large number of biosensor devices over an area of $\sim 1 \text{ m}^2$.

We have designed an optical testbed with area illumination and imaging detection and used it for a target distance of about 3 feet. Restricting the illuminated and imaged area to about 1 cm^2 was extremely beneficial for the brightness evaluation of optical tags, since it permitted us to distinguish between individual tags (Figure 16).

The key result is that one tag ($1 \mu\text{m}$ Nile-red FluoSphere, Molecular Probes Inc., product nr. F-8819) in the detection area of the device is sufficient to produce a detectable signal at the specified device coverage ($10\text{-}100 \text{ dev./spot} = 10^3 \text{ dev./m}^2$) and stand-off distance (500 m).

We further compared the brightness of Nile-red FluoSpheres with quantum dot virus nanoparticles (QD-VNP) prepared by Amy Szuchmacher-Blum and Banahalli Ratna from the Naval Research Laboratory (see A.S. Blum et al., Small 2005, 1, p. 702-706) using a fluorescence microscope (Nikon TE2000 with Andor IXON camera). Normalized to an equal excitation intensity, a QD-VNP appeared to have 20-30% of the brightness of a FluoSphere.

We are continuing to use this setup to determine the detection efficiency for optical tags encapsulated in transparent microdevices (Figure 15), and, once we have found a satisfactory method to produce microdevices integrating motor proteins and optical tags, to image multiple devices over large areas as originally planned.

A publication describing the results in detail is in preparation and will be referenced in the final report of the continuation grant FA9550-05-1-0366.

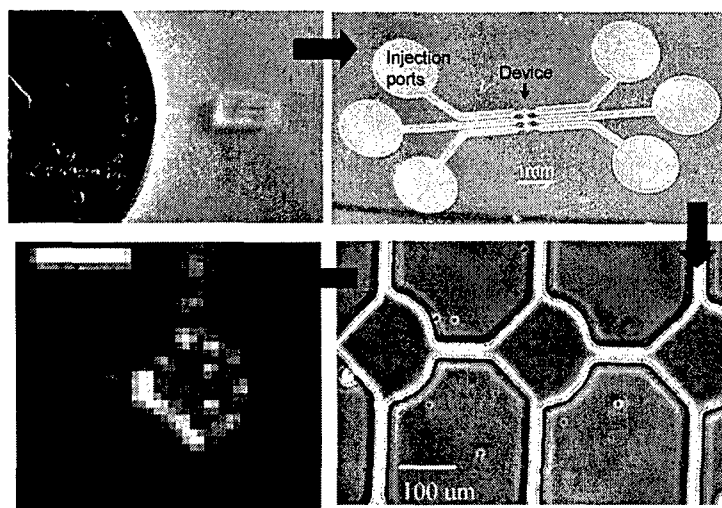


Figure 15: Design of polymeric microdevices at different scales, and imaging of FluoSpheres in the detection chamber using the testbed.

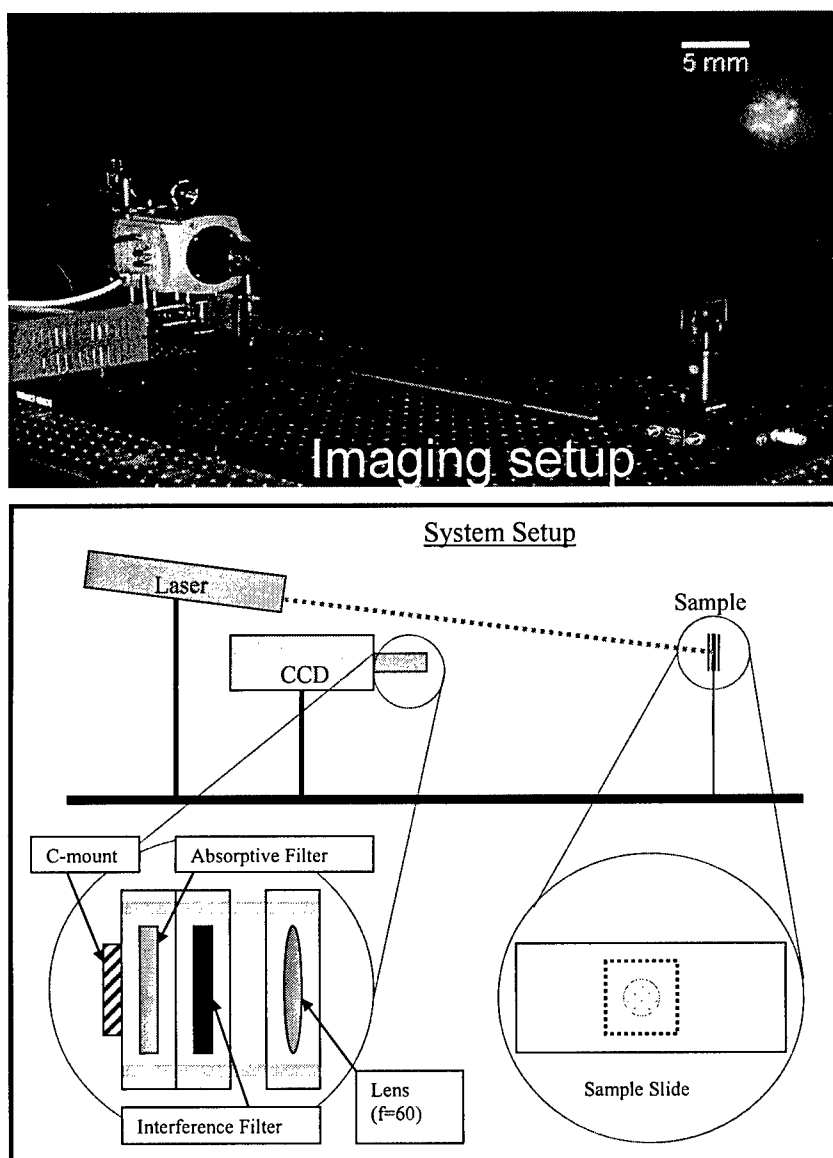


Figure 16: The testbed with imaging detection as it is being used to evaluate the brightness of fluorospheres. The camera, laser and sample are all attached to an optical table. The laser (532 nm) runs through a 10X beam expander (Edmund Optics NT55-578) and is aimed over the CCD camera to minimize the incident angle of the beam on the sample. The lens and filter system is assembled using the LINOS microbench system. The absorptive filter (Newport, KV-550) is placed behind the interference filter (Chroma, HQ595_50m). The system has a C-mount, which screws into the camera, and four rods through small square plates. The plates can move along the rods, allowing for the adjustment of the lens (LINOS, 06 3045), while the filters remain secured in front of the CCD. The entire unit is wrapped in black foamcore and then taped using black optical tape (3M, 235) to shield from extraneous light.

Task 3.1 *Storage methods for biomolecular motor-powered nanodevices.*

The methods and results are publicly accessible through: R. Seetharam, Y. Wada, S. Ramachandran, H. Hess, P. Satir: "Long-term storage of bionanodevices by freezing and lyophilization", Lab on a Chip 2006, DOI:10.1039/B601635A

Abstract: Flow chambers retained MT motility after snap freezing in liquid nitrogen. They needed no additional ATP when thawed immediately and observed under the microscope or stored at -80°C for 48 h. Streptavidin coated biotinylated microtubules were also found to be stable and retain motility after snap freezing. In addition, the anti-myoglobin antibody bound to biotinylated microtubules via streptavidin retained its ability to bind to myoglobin, which was detected with a secondary FITC-labeled antibody. The lyophilization of motility assays in glass flow cells was also successful. Freezing introduced variability of MT preservation and motility but smaller flow cells had more uniform distribution of microtubules. Lyophilized chambers retained MT motility after addition of fresh motility buffer with ATP (Fig. 17) or when reconstituted with water. The degradation of microtubules upon lyophilization was reduced when trehalose was used in the chamber. These experiments demonstrate that complete bionanodevices integrating large protein assemblies, such as microtubules, as well as highly functional molecular machines, such as kinesin motors, can be stored for extended periods of time and returned to an active functional state by thawing or rehydration.



Figure 17: Images of microtubule motility in a kinesin driven system from 0 (red) to 10s (green) after rehydration following lyophilization and storage for 14 days of a self contained chamber. This procedure separates biomolecular nanodevice assembly from utilization.

Task 3.2 Computer-assisted design and prediction of performance of guiding structures for molecular shuttles.

The methods and results are publicly accessible through: T. Nitta, A. Tanahashi, M. Hirano, H. Hess: "Simulating molecular shuttle movements: Towards computer-aided design of nanoscale transport systems", Lab on a Chip, DOI: 10.1039/b601754a, webpublished 5/31/06

Abstract: Molecular shuttles based on the motor protein kinesin and microtubule filaments have the potential to extend the Lab-on-a-chip paradigm to nanofluidics by enabling the active, directed and selective transport of molecules and nanoparticles. Based on experimentally determined parameters, in particular the trajectory persistence length of a microtubule gliding on surface-adhered kinesin motors, we developed a Monte-Carlo simulation, which models the transport properties of guiding structures, such as channels, rectifiers and concentrators, and reproduces the properties of several experimentally realized systems. Our tool facilitates the rational design of individual guiding structures as well as whole networks, and can be adapted to the simulation of other nanoscale transport systems.

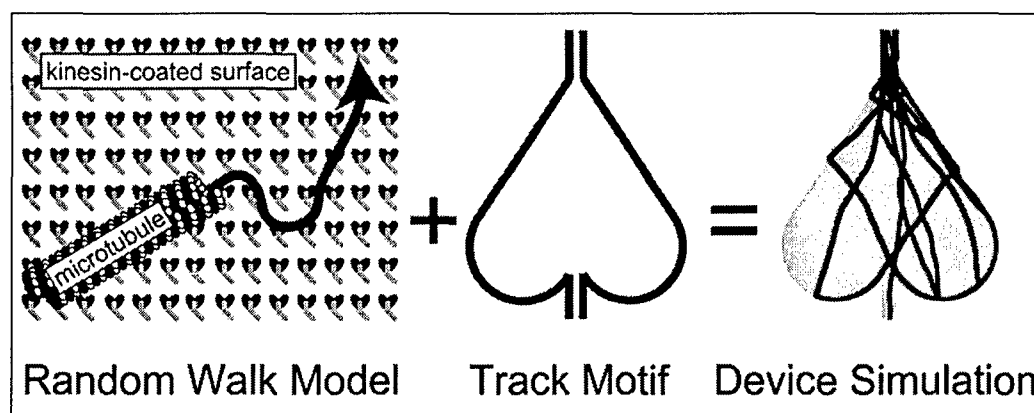


Figure 18: A new simulation tool enables rational design of microfluidic devices integrating biomolecular motors. The simulations reproduce the behavior of devices described in the literature and can be used for failure analysis of existing devices and design of new structures.